Study on the role of soot and heat fluxes in upward flame spread using a wall resolved large eddy simulation approach

Kazui Fukumoto[a,b], Changjian Wang[a,†], and Jennifer X. Wen[b,‡]

[a] School of Civil Engineering, Hefei University of Technology, Hefei, 230009, China

[b] School of Engineering, University of Warwick, Coventry, CV4 7AL, United Kingdom

[c] Anhui International Joint Research Centre on Hydrogen Safety, Hefei, 230009, China

Abstract

The present study aims to obtain further understandings of vertical flame spreading phenomena by analysing the influences of soot and individual heat flux components on PMMA walls using large eddy simulation. Total heat flux consists of convective and radiative components, but it is not clear which one has a significant role in fire spread. The computational code used is an in-house version of FireFOAM 2.2.x, which has recently undergone specific development and validation for flame spread studies by the authors. The present study has conducted numerical simulations for flame spread and full wall fire configurations. By scale-up of the PMMA size from 0.4 to 1.0 m, the convective heat flux decreased by 41.4% at the location of the pyrolysis front, radiative heat flux increased by 86.9%, and radiative heat flux due to soot grew by 215.2%. As the pyrolysis height increases from 0.3 to 1.0 m, the convective heat flux decreased by 26.8% at the location of the pyrolysis front. The radiative heat flux increased by 96.8%, and its components of combustion of the gaseous fuel and soot grew by 55.9% and 233.3%, respectively. Moreover, the ratio of radiative heat flux to total heat flux increased by 66.5%, and that of soot to radiative heat flux grew by 73.9%. The contribution of soot to radiative heat flux almost linearly increased against the pyrolysis height, and that was higher at a higher pyrolysis height.

Article highlights

Corresponding authors: †chjwang@hfut.edu.cn ‡Jennifer.Wen@warwick.ac.uk

✓ The radiative heat flux increases by 86.9%, expanding 0.4–1.0 m of the PMMA size near the pyrolysis front.

✓ The radiative heat flux increases by 96.8% between pyrolysis height = 0.3–1.0 m near the pyrolysis front.

✓ The contribution of soot to radiative heat flux increases by 73.9% between $x_p \approx 0.3$–1.0 m near the pyrolysis front.

Nomenclature

a_{rad} absorption coefficient [1/m]

A frequency factor (unit is dependent on a equation)

Cp specific heat at constant pressure [J/(K·kg)]

C_{D2} model constant of the eddy dissipation concept

C_S Smagorinsky constant

C_w model constant of wall adapting local eddy viscosity model

d wall thickness [m]

E activation energy [kJ/mol]

Err error (%)

f_v soot volume fraction

h enthalpy [J/kg]

Δh enthalpy of formation [J/kg] or [J/mol]

Δh_{comb} heat of combustion [J/kg] or [J/mol]

H PMMA height [m]

k (total) turbulent kinetic energy [m^2/s^2]

m'' local pyrolysis rate [kg/(s·m^2)]

$\dot{m}^*$ mass transfer rate between fine structure and surrounding fluids [kg/s]

p pressure [Pa]

Pr_t	turbulent Prandtl number
q'	heat release rate scaled by wall width [W/m]
q''	heat flux [W/m^2]. Section 2.5.1 presents several definitions.
r_{rad}	reflectivity
R	gas constant [kJ/((mol·K))]
R_0	criterion of flame volume
s	stoichiometric oxygen-fuel mass ratio
S_S	soot particulate surface area [m^2/kg]
Sc_t	turbulent Schmidt number
t	time [s]
T	temperature [K]
T_a	activation temperature [K]
W	PMMA width [m]
x, y, z	coordinates [m] or the number of elements C, H, and O in a chemical equation
x_p	pyrolysis height [m]
x_f	flame height [m]
x_{wall}	distance from the bottom leading edge of PMMA [m]
$y_{standoff}$	standoff distance [m]
Y	mass fraction
Z	mixture fraction

Greek

γ	mass fraction of fine structures
ε	(total) dissipation rate [m^2/s^3]
ε_{rad}	emissivity
η_{rad}	transmissivity

Δy_{wall} width of grid cell next to wall [mm]

λ heat conductivity [W/(K·m)]

v kinematic viscosity [m²/s²]

ξ Criterion of flame regions

ω reaction/pyrolysis rate [kg/(s·m³)]

ρ density   [kg/m³]

σ_{Stefan} Stefan-Boltmann constant [W/(m²·K⁴)]

τ time scale [s]

τ_η Kolmogorov time scale

ϕ equivalence ratio

χ reaction fraction in the fine structures

subscripts

chem   chemical reaction

conv   convection

diff   diffusion

EDC   eddy dissipation concept

em   emitted

fu   fuel

first   first cell

gas   gas/gasification

integ   integral

inter   interface

J chemical species

mel   melting

mod   modified

net   net

ox   oxidiser or oxygen

p   pyrolysis

pr   product

rad   radiation/radiative

refl   reflective

res   revolved

solid   solid

S/soot   soot

SGS   sub-grid scale

tot   total

vap   vaporisation

wall   wall

0   reference or standard value

Superscript

*   fine structures

0   surrounding fluids

bar

$\bar{\phi}$ time average variable

$\tilde{\phi}$ density weighted average variable

1. **Introduction**

Upward flame spread is an essential topic in fire safety owing to its relatively faster spread rate than horizontal, downward or inclined fire spreading. Many investigators have studied the upward flame spread phenomenon [1–7]. Drysdale and Macmillan [2] reported that the flame spread rate on the surface at 30 degree increased fivefold compared with horizontal fire spread in the presence of sidewalls and twofold without sidewalls. Some previous studies focused on underlying heat transfer

and reported the wall heat fluxes in the flame spread phenomena. Orloff et al. [3] concluded that the radiation contribution was 75 to 80% of total heat transfer to the polymethyl methacrylate (PMMA)-surface at heights between 76–152 cm. Tsai [4] studied the influence of sidewalls and width. They found that the flame height and fire spread rate were higher for the wider PMMA walls but did not observe a significant difference in the total heat fluxes for different sample widths. Hasemi [5] experimentally investigated the correlation of heat transfer for upward flame spread and found that a wall above the fire source could be divided into four regions which are characterised by the thickness and intermittency of a luminous flame, namely, the lower and upper parts of the stable fire, as well as the transition and smoke areas. The effect of the altitude on flame spreading in the vertical direction was examined by Liang et al. [6], who reported that the flame spread rate at higher altitude was slower than that at low altitude due to the relatively lower heat flux under lower ambient pressure. Singh and Gollner [7] experimentally investigated local mass burning rates and heat fluxes on a laminar boundary layer over methanol, ethanol and PMMA. They found that the convective heat flux was nearly 85–90% of the total heat flux and a radiative component was never more than 20% in the laminar boundary layer. Consalvi et al. [8] performed two dimensional (2-D) numerical simulations of upward fire spread over PMMA wall. They made predictions for total as well as incident radiative and convective heat fluxes but provided only comparison with experimental data and detailed discussion for total heat flux. Karpov et al. [9] performed a 2-D numerical analysis of flame spread along a PMMA slab using large eddy simulation (LES) techniques with solid-phase pyrolysis modelling to investigate radiative and convective heat fluxes. They reported pulsating heat flux in the transition area between laminar and turbulent flame.

The pyrolysis modelling of PMMA is relatively easy owing to a no charring material, but its coupled simulation with the gas phase is still challenging owing to the complexity of underlying physics during fire spread. As reported in a previous study [3], laminar-turbulence transition occurs at 0.18 m from the bottom of a wall; therefore, the effect must be taken into account in turbulence and combustion

modelling. PMMA is a sooty fuel; the soot formation and oxidation models must be considered with radiation calculation. Some numerical and experimental investigations reported a convex shape of the pyrolysis front for a flame spread configuration without side walls [1,6], which cannot be simulated by 2-D flame spread modelling. Furthermore, relatively complex experimental geometries such as a corner wall configuration require 3-D combustion simulation [10], leading to the enormous computation cost. Some limited computational studies based on coupled fluid-solid approaches in 3-D configurations have also been performed in recent years. Liao and T'ien [11] numerically investigated ignition and flame spread on a composite solid fuel based on a 3-D model coupled with the solid phase simulation to capture some fine details of the ignition and flame spread processes. Their model was later extended by Zhao and T'ien [12] to analyse fire spread and extinction in a concurrent flow. Tseng and T'ien [12] and Zhao and T'ien [11] focused on short composite slabs, and thus the flows were laminar.

To overcome the above problems, the authors have previously reported [1] some 3-D analyses of vertical flame spread on PMMA using an in-house version of FireFOAM [13], a computational code for fire simulation within the frame of OpenFOAM [14]. The present study uses this FireFOAM that incorporates the recently developed and modified sub-models for combustion, soot and radiation treatment [15–17]. Some modifications were also introduced to consider laminar-turbulent transition, in-depth radiation in the PMMA slabs and regression of the PMMA surface. Validations were conducted with the pyrolysis cases of Pizzo et al. [18], the fire spread measurements of Huang and Gollner [19] and Liang et al. [6], as well as soot measurements of Hebert et al. [20]. Because of the complexity of underlining physics, the authors reported a sensitivity study on modelling for laminar-turbulent transition for combustion, radiation, ignition, and soot formation/oxidation. Also, the previous study [1] reported several data of flame spreading such as the pyrolysis and flame heights, flame spread rate, total heat flux, the heat release rate, and velocity. Similarly, the predicted 3-D flame volume and vortex structures were analysed.

Namely, the previous study reported the framework of flame spread modelling, general topics of flame spread on a PMMA wall, selection of sub-models, model parameters, and its validation. In terms of these topics, the reader should refer to the authors' previous publication [1]. In contrast, the present study only focuses on the themes of heat fluxes, e.g. the blowing effect, soot influence, and temperature distribution. The present study mostly deals with (i) analysing the specific individual heat flux components and (ii) the influence of soot on flame spreading, as well as (iii) considering finite rate chemistry in flame spread modelling and reporting its effect on the predictions. Several experimental and numerical studies analysed relative magnitudes of the total, convective, and radiative heat fluxes and the influences of those [3,9] for flame spreading scenarios. Despite the above progress, none of the previous studies respectively evaluated radiative heat fluxes due to combustion gas and soot, or which insight is still lacking despite their significance as driving force. The present analysis splits the radiative heat flux into gas and soot components and evaluates its impact on flame spread at the locations of the pyrolysis front and flame tip. Total heat flux consists of convective and radiative components depending on their source; hence, their evolution trends seem to be different with the progress of fire growth. Although soot is considered a critical factor in fire spread owing to the notable impact on radiative heat flux, it has not been clear how soot influences and accelerate flame spread rate yet. In terms of flame spread modelling, the present study updates the finite-rate chemistry from infinitely fast chemistry for both gas-phase combustion and soot oxidation. Many previous studies utilised infinitely fast chemistry for flame spread and fire simulations [1,8,21,22]. However, finite-rate chemistry with a one-step chemistry model can be an alternative chemistry treatment owing to its lower computation cost.

In the present paper, a medium-scale full wall fire scenario (0.4 m in height) of Hebert et al. [20] was investigated to test the model's sensitivity and accuracy of f_v. Furthermore, the simulation of a relatively taller full wall fire (1 m in height) was conducted, and the predictions were compared with the measurements of Orloff et al. [3]. Finally, predictions for the upward flame spread scenarios

8

without side walls (1 m high) of Liang et al. [6] were used to discuss the influences of the heat fluxes and soot on flame spread.

The results were analysed to shed light on the relative magnitudes and contributions of individual heat flux components to total heat flux and overall fire spread. The radiative heat fluxes owing to soot and gases were distinguished, and relative importance of radiative heat flux due to soot on flame spread was discussed.

2. Methodology

2.1. Overview of the numerical solver

The present study uses the in-house version of the LES based FireFOAM solver. The previous study described further details about modifications to facilitate flame spread study [1] or an appendix in this study [27] describes the numerical treatments. The central linear scheme is applied to the momentum equation, and the linear scheme limited by total variation diminishing is employed to the sensible enthalpy and mass fractions equations. The discretisation scheme for time integration is the second-order backward differential scheme. The momentum and pressure coupling scheme is the Pressure Implicit with Splitting of Operator (PISO) algorithm with outer iteration, termed PIMPLE in OpenFOAM [14]. The number of outer iteration is 2, following the authors' study [1].

k_{SGS} must be close to zero near the wall, and so the sub-grid scale modelling for LES is the wall-adapting local eddy-viscosity (WALE) model with the model constant $C_w = 0.55$ [23]. The WALE model does not contain the estimation of k_{SGS}, and so the authors previously estimated k_{SGS} [1] as $k_{SGS} = 0.5|\mathbf{u_{SGS}}|^2$, and $|\mathbf{u_{SGS}}| = v_{SGS}/(C_S\Delta_{filter})$ where $C_S = 0.18$ following Nicoud et al. study [23] which suggested that this C_S value linked $0.55 \leq C_w \leq 0.60$. The authors previously validated the velocity profile in the upward direction with the law of the wall, including the blowing effect [1].

Combustion is modelled using Chen et al.'s EDC model [15,16] incorporating the laminar-turbulence transition treatment, which improves the predictions of heat flux [1]. The

pyrolysed PMMA is considered as methyl methacrylate (MMA) $C_5H_8O_2$ and the gas-phase reaction is treated as a one-step overall reaction. Based on Tarrazo et al. [24], the finite reaction rate is newly applied to gas-phase combustion, and their scheme is introduced in Section 2.3.

As reported in our previous study [1], the laminar-turbulent transition occurs at $x_{wall} \approx 0.18$ m. The criterion for the laminar-turbulence transition for the combustion model is used following our previous study [1]. This combustion model involves the time scale estimated by viscous diffusion τ_{diff} [1] and that based on turbulent diffusion τ_{EDC} calculated by Chen et al.'s EDC model [15,16]. $\tau_{diff} > \tau_{EDC}$ means stronger turbulent diffusion than laminar diffusion. Conversely, $\tau_{diff} \leq \tau_{EDC}$ indicates laminar diffusion is stronger than turbulent diffusion. Assuming that stronger diffusion is responsible for chemical reaction, the above criterion divides turbulent combustion region and laminar combustion region. Appendix in this study [27] gives further specific descriptions.

For radiative heat transfer, the FireFOAM solver uses the finite volume discrete ordinate method with the weighted sum of grey gases (WSGG) model [25] for gases radiative properties; radiation intensity is discretised by a total of 48 angles following Zeinali et al.'s study [10]. The authors compared the radiative heat flux obtained by several radiation sub-models and confirmed that the WSGG model provided better results [1]. The procedure to calculate the mean beam length is given in supplemental materials [27]. The absorption coefficient of soot is the constant Plank mean absorption coefficient following Consalvi et al. [8].

The soot formation model is Chen et al.'s development [15] based on the partially stirred reactor (PaSR) concept and the smoke point height = 0.105 m. The soot oxidation treatment is Wang et al.'s model [26] that includes finite-rate chemistry. The authors' previous study showed the sound prediction of the soot volume fraction, assuring the effect of soot on radiative heat flux. The viscosity is calculated by the Sutherland law [14], λ is obtained by the modified Eucken correlation [28], and Cp is calculated by the 7-coefficient NASA's polynomials using Burcat's database [29]. Pr_t and Sc_t are set to 0.85.

For model parameters used in the gas phase, please refer to Fukumoto et al. [1]. For the description of flame spread modelling, the reader should refer to the supplemental materials [27], and the authors' recent publication reported validation and sensitivity tests for sub-models [1]. The following sections describes only the newly implemented sub-models.

2.2. EDC with finite-rate chemistry

For turbulent combustion ($\tau_{\text{diff}} > \tau_{\text{EDC}}$), the reaction rate is estimated by Gran et al.'s EDC model [31]. Their model divides a region into fine structures and surrounding fluids, assuming that reaction takes place only in the fine structures. The fine structures are considered to be a PaSR, and the following equation is computed until reaching the steady-state solutions, with the current density, mass fractions, and temperature in respective computational cells

$$\frac{dY_J^*}{dt} = \frac{\omega_J^*}{\bar{\rho}} + \dot{m}^*(Y_J^0 - Y_J^*),$$ (1)

where Y_J^* is the mass fraction of chemical species J in the fire structures, ω_J^* is the reaction rate of chemical species J in the fine structures computed by the Arrhenius equation, and Y_J^0 is the mass fraction of chemical species J in the surrounding fluids. $\dot{m}^*$ corresponds to the mixing rate of the PaSR, which is given by Chen et al.'s extended EDC model [16] as

$$\dot{m}^* = \left(\frac{3}{C_{\text{D2}}}\right)^{1/2}\left(\frac{\varepsilon}{\nu}\right)^{1/2},$$ (2)

where $C_{\text{D2}} = 0.75$.

In the EDC model, $\tilde{Y}_J$, Y_J^*, and Y_J^0 are given as

$$\tilde{Y}_J = \gamma\chi Y_J^* + (1.0 - \gamma\chi)Y_J^0,$$ (3)

where γ and χ are obtained by the extended EDC model, and Y_J^0 is obtained by Eq. (3)

The time average reaction rate of chemical species J is given as

$$\bar{\omega}_J = \bar{\rho}\dot{m}^* \frac{\gamma\chi}{1-\gamma\chi}(Y_J^* - \tilde{Y}_J) \quad \text{kg/(s·m}^3\text{)},$$ (4)

11

where Y_J^* is the solution of Eq. (1).

For laminar combustion ($\tau_{\text{diff}} < \tau_{\text{EDC}}$), the following equation is integrated between $t = 0$ and Δt s.

$$\frac{dY_J}{dt} = \frac{\omega_J}{\rho}.$$
(5)

The time average reaction rate of chemical species J is given as

$$\bar{\omega}_J = \frac{\bar{\rho}(Y_{J,t+\Delta t} - \tilde{Y}_J)}{\Delta t} \quad \text{kg/(s·m}^3\text{)},$$
(6)

where $Y_{J,t+\Delta t}$ is the solution of Eq. (5).

2.3. Reaction scheme

Tarrazo et al. [24] suggested an irreversible one-step chemistry model for hydrocarbon fuels and validated its results with a methane-air counterflow. The model can predict the critical strain rate at extinction as well as near extinction flames with oxygen leakage. Tarrazo et al.'s one step chemistry is given as

$$C_xH_yO_z + (x + \frac{y}{4} - z)O_2 = xCO_2 + \frac{y}{2}H_2O - \Delta h_{\text{comb,mod}},$$
(7)
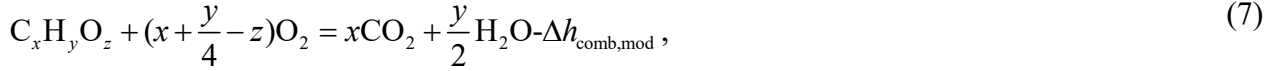
where $\Delta h_{\text{comb,mod}}$ is the modified Δh_{comb} according to the equivalence ratio, and Δh_{comb} of pyrolised PMMA is 2.42×10^7 J/kg [6] ($\approx 2.42 \times 10^3$ kJ/mol).

The global formation rate is given as

$$\omega_{\text{fu}} = A \exp(-\frac{T_a}{T})[C_xH_yO_z][O_2] \quad \text{mol/(s·cm}^3\text{)},$$
(8)

where $A = 6.9 \times 10^{14}$ cm^3/(mol·s), [] indicates the molar concentration [mol/cm^3]. Tarrazo et al. [24] gives T_a according to a change in the equivalence ratio as

$$\begin{cases} \phi \leq 0.64: & T_a / T_{a,0} = 1 + 8.25(\phi - 0.64)^2 \\ 0.64 \leq \phi \leq 1.07: & T_a / T_{a,0} = 1 \\ \phi \geq 1.07: & T_a / T_{a,0} = 1 + 1.443(\phi - 1.07)^2 \end{cases},$$
(9)

where the reference activation temperature $T_{a,0} = 15{,}900$ (K).

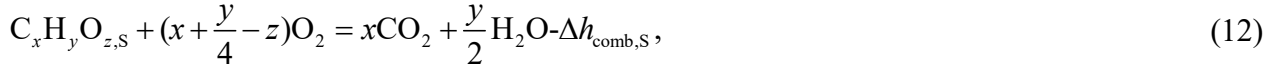$\Delta h_{\text{comb,mod}}$ is depending on the equivalence ratio:

$$\begin{cases} \phi \le 1 : \Delta h_{\text{comb,mod}} / \Delta h_{\text{comb}} = 1 \\ \phi \ge 1 : \Delta h_{\text{comb,mod}} / \Delta h_{\text{comb}} = 1 - \psi(\phi - 1) \end{cases} \tag{10}$$

where ψ is the constant variable which is dependent on different hydrocarbons [24]:

$$\psi = -[\Delta h_{\text{C}x\text{H}y\text{O}z} - x(\Delta h_{\text{CO}_2} - 2\Delta h_{\text{H}_2\text{O}})] / \Delta h_{\text{comb}} . \tag{11}$$

2.4. Soot oxidation model

Our previous study [1] used Chen et al.'s soot model [15], applying the infinitely fast chemistry assumption in the computation of the soot oxidation rate. Wang et al. [26] recently removed this assumption in Chen et al.'s soot oxidation model and reported the improvement in the prediction accuracy. Therefore, the present flame spread modelling adopts Wang et al.'s model. Wang et al.'s model gives the reaction of soot oxidisation as

$$\text{C}_x\text{H}_y\text{O}_{z,\text{S}} + (x + \frac{y}{4} - z)\text{O}_2 = x\text{CO}_2 + \frac{y}{2}\text{H}_2\text{O-}\Delta h_{\text{comb,S}} , \tag{12}$$

where $\Delta h_{\text{comb,S}}$ is the heat of combustion of the particle of soot. $\Delta h_{\text{comb,S}}$ is computed as $\Delta h_{\text{comb,S}} = \Delta h_{\text{comb}}$, where Δh_{comb} is considered as Δh_{comb} of $\text{C}_x\text{H}_y\text{O}_{z,\text{gas}}$.

Yao et al. [32] estimated the soot oxidisation rate following previous researches [33,34] and found it to be negligible below 1,300 K:

$$\omega_{\text{S,ox}} = \begin{cases} A_{\text{S,ox}}[\text{O}_2]T^{0.5} \exp\dfrac{-E_\text{S}}{RT} \rho Y_\text{S} S_\text{S} & 0 \le \widetilde{Z} \le Z_{\text{ox}} \text{ and } T \ge 1,300 \ K \\ 0 & \text{else} \end{cases} \quad \text{kg/(s·m}^3\text{)}, \tag{13}$$

where $A_{\text{S,ox}} = 120$ kg·m/(mol·K$^{0.5}$) [32,34], $E_\text{S} = 163.54$ kJ/mol [32,34], [O$_2$] is the mole concentration of O$_2$ [mol/m^3], Z_{ox} is the critical mixture fraction for soot oxidation estimated as $Z_{\text{ox}} = \widetilde{Z}$, and $S_\text{S} = 160{,}000$ m^2/kg suggested by Yao et al. [32].

Also, Wang et al. [26] estimated the time averaged soot oxidation rate by the PaSR concept given as

$$\bar{\omega}_{\text{S,ox}} = \frac{\tau_{\text{S,ox,chem}}}{\tau_{\text{S,ox,chem}} + \tau_{\text{mix}}} \omega_{\text{S,ox}} \quad \text{kg/(s·m}^3\text{)}. \tag{14}$$

13

where $\tau_{S,ox,chem}$ is the chemical reaction time scale of oxidation of soot given as

$$\tau_{S,ox,chem} = \min\left(\frac{\overline{\rho}\tilde{Y}_S}{\omega_{S,ox}}, \frac{\overline{\rho}\tilde{Y}_{O_2}}{s\omega_{S,ox}} \right) \quad s. \tag{15}$$

Pevious studies [1,15,26] gives τ_{mix} as

$$\tau_{mix} = \sqrt{\tau_\eta \tau_{integ}} = \sqrt{\left(\frac{\nu}{\varepsilon}\right)^{0.5}\left(\frac{k}{\varepsilon}\right)} \quad s, \tag{16}$$

where τ_η is the Kolmogorov time scale and τ_{integ} is the integral time scale. The estimations of k and ε are on the basis of Chen et al.'s EDC model [15,16].

2.5. Solid phase model

2.5.1. Medium-scale full wall fire scenario
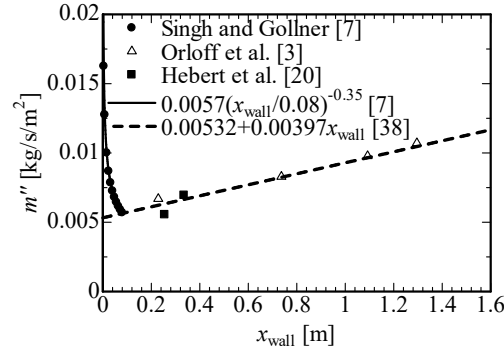
Fig. 1 Local mass-loss rate m'' under the full wall fire state on the PMMA surface.

The previous full wall fire simulation [1] needed to be run for a real-time of 1840 s to capture the whole process of the experiment. This long simulation was because Hebert et al. [20] measured the soot volume fraction from 1840 s. However, the simulation would be computationally costly. Several previous measurements [7,20,38] presented the local mass-loss rate, and the present simulation used those to save the computation time. The previous simulation was the fully gas-solid coupled approach [1]. However, since the mass-loss rate is known, the present simulation does not need the solid-phase simulation. Figure 1 shows the local mass-loss rate during a full wall fire scenario on the PMMA surface:

14

$$m'' = 0.0057(x_{wall}/0.08)^{-0.35} \quad 0.08\,\text{m} > x_{wall}$$
$$m'' = 0.00532 + 0.00397x_{wall} \quad 0.08 < x_{wall} < 3.56\,\text{m} \qquad \text{kg/(s·m}^2). \tag{17}$$

(a) Medium-scale full wall fire

(b) Large-scale full wall fire
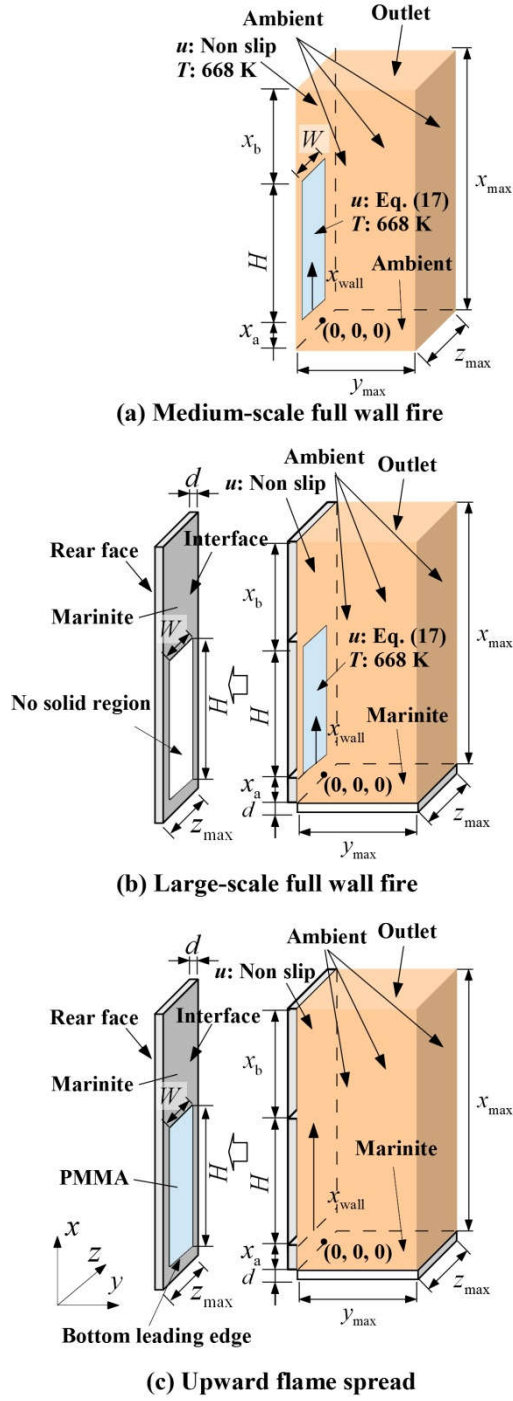
(c) Upward flame spread

Fig. 2 Computational domains for respective scenarios. The right is the gas region, and left is solid region.

15

The PMMA heights of Orloff et al. [3] and Hebert et al.[20]'s experiments were different from that of Orloff et al.'s experiment [38], but both the mass-loss rates were similar to the reproduction by Eq. (17). The surface temperatures on the PMMA and marinite walls were set to 668 K following the pyrolysis temperature of PMMA used by Singh and Gollner [7]. The computation of the wall temperature on the marinite wall until the steady-state is computationally expensive. Using $T = 668$ K and m'' in Eq. (17) as an inlet condition, the simulation of the solid region is no longer needed. It is noteworthy that the temperature on the marinite wall is slightly higher than the realistic value owing to no pyrolysis.

Notably, a higher level of soot formation/oxidation will mean a higher level of heat fluxes. In practice, this would increase the release of pyrolysis gases and would results in a higher $q''_{rad,gas}$ than that without the presence of soot. As the full wall fire simulations use the experimental mass-loss rate (i.e. Eq. (17)), they are not affected by this dependence of the $q''_{rad,gas}$ on the soot formation, thereby allowing to quantify the level of heat flux change in presence/absence of soot in the simulations.

The PMMA size was $H \times W \times d = 0.4$ m $\times$ 0.2 m $\times$ 0.03 m, where x_{max} was 0.96 m, y_{max} was 0.25 m, z_{max} was 0.248 m, x_a was 0.05 m, x_b was 0.51 m, and $x_{wall} = x - x_a$ in Fig. 2. For all the solid phases (PMMA and marinite), the division number in the depth direction was 210 grid cells. In Fig. 2(a), a total pressure condition was assigned on the ground and sides to allow inflow. The present simulations prepared 297,600 grid cells for the gas phase and 1,249,920 grid cells for the solid phases. The base grid sizes were $\Delta y_{wall} = 1$ mm with the expansion ratio $\approx 6\%$, and uniform $\Delta x = 5$ mm and $\Delta z = 8$ mm in the gas region. However, the total cell number for the gas phase was slightly changed in grid dependency tests to keep the expansion ratio of 6%. Also, the quantities were time-averaged for 30 s.

2.5.2. Large-scale full wall fire scenario

This scenario also provided the empirical mass-loss rate in Eq. (17). It applied $T_{\text{wall}} = 668$ K on the PMMA wall but removed the simple treatment of the adiabatic condition on the marinite wall used in our previous study [1]. Although this treatment is not necessary, it can give a realistic gas temperature on the marinite wall.

The respective model parameters for the marinite wall are: $\rho_{\text{solid}} = 800$ kg/m^3 [37], $\lambda_{\text{solid}} = 0.1154$ W/m/K [37], $Cp_{\text{solid}} = 1110$ J/kg/K [37], $r_{\text{rad,solid}} = 0.02$ $(= 1 - \alpha_{\text{rad,solid}} - \eta_{\text{rad,solid}})$, $\alpha_{\text{rad,solid}} = 0.98$ [37], $\varepsilon_{\text{rad,solid}} = 0.98$, $\eta_{\text{rad,solid}} = 0$ and $\lambda_{\text{inter}} = \lambda_{\text{gas}}$ where λ_{gas} is estimated by the modified Eucken equation [28]. ω_{solid} is set to 0 owing to an inert material. The model parameters for PMMA were presented in the previous study [1], but $\lambda_{\text{inter}} = \lambda_{\text{gas}}$ on the PMMA surface is used in order to ensure consistency of q''_{conv} estimation for the marinite and PMMA.

The specific dimensions in Fig. 2(b) were the same as Liang et al.'s experimental scenario for comparison in Section 3.3.2. In Fig. 2(b), the PMMA size was $H \times W \times d = 1.0$ m $\times$ 0.304 m $\times$ 0.01 m; and x_{max} was 1.9 m, y_{max} was 0.7 m, z_{max} was 0.36 m, x_{a} was 0.005 m, and x_{b} was 0.895 m. The grid sizes (Δy_{wall}, Δx and Δz) were $\Delta y_{\text{wall}} = 1$ mm with the expansion ratio $\approx 6\%$, and uniform $\Delta x = 5$ mm and $\Delta z = 8$ mm in the gas region. In all the solid regions, the division number in the depth direction was 70 uniform cells. A ground was treated as the marinite wall in Fig. 2. The total cell numbers were 1,197,000 for the gas phase and 1,417,500 for the solid phases. Equation (17) gives m''. The temperature on the PMMA wall was set to 668 K, while the pyrolysis model computed T on the marinite wall. The physical time in this simulation was until $t = 175$ s to obtain the approximately steady temperature on the marinite wall, and the period of the average data was between $t = 145$–175 s.

2.5.3. Upward flame spread scenario

On the PMMA surface, the 1-D diffusion sensible enthalpy equation was applied with the pyrolysis rate estimated by the expression of the Arrhenius type [35]. In-depth radiation was incorporated by Beer's law [36]. For surface regression modelling, the volume-loss rate and surface-regression length were assumed to be proportional to the mass-loss rate. The authors previously conducted a solid-phase simulation to validate the developed pyrolysis model with the experimental data of Pizzo et al. [18]. The readers refer to the authors' previous paper about the validation study [1] and the solid phase model description in the appendix [27]. On the marinite wall, this scenario uses the same assumption and parameter in Section 2.5.2.

In Fig. 2(c), the PMMA size was $H \times W \times d = 1.0$ m $\times$ 0.304 m $\times$ 0.01 m; and x_{max} was 1.9 m, y_{max} was 0.7 m, z_{max} was 0.36 m, x_a was 0.005 m, and x_b was 0.895 m.

The cell sizes (Δy_{wall}, Δx, and Δz) were the same as the previous section. In all the solid regions, 70 cells were uniformly used in the depth direction. Grounds were treated as the marinite wall in Fig. 2. The total cell numbers were 1,197,000 for the gas phase and 1,417,500 for the solid phases. Giving incident q''_{rad} of 45 kW/m^2 for 75 s heated the wall at $0 \leq x_{wall} \leq 0.005$ m. After that, a small fire developed next to the wall by the combustion model with infinitely fast chemistry for ignition. The thickness of this initial small fire is about 5–7 mm, where the thickness is the maximum coordinate in the y-direction with the highest temperature. The time was set to zero after confirming the fire was sustained. The authors suggested that the ignition length significantly influenced the initial heat release rate and flame height. In other words, the determination of the ignition length should be dependent on the agreement of the flame height or the heat release rate with the measured data.

The previous investigators determined a pyrolysis front by temperature [6–8]. Thus, the pyrolysis temperature was defined as 580 K at 0.5 mm from the front interface ($y = -0.0005$ m) following our previous study [1].

18

2.6. Heat flux terminology

The present study focused on heat fluxes. Respective terms are the incident radiative heat flux q''_{rad}, convective heat flux q''_{conv}, and emitted radiative heat flux q''_{em}. The present study employs the finite volume discrete ordinate method in OpenFOAM with the weighted sum of grey gases (WSGG) model [25] and descretises radiation intensity with a total of 48 angles. The sum of radiation rays going to the wall is q''_{rad} and that emitted from the wall is q''_{em}, where q''_{em} is the sum of the reflective radiative flux and surface emission:

$$q''_{em} = q''_{refl} + \sigma_{Stefan} T_{wall}^4 \qquad \text{W/m}^2 \qquad (18)$$

where q''_{refl} the reflective radiative flux that is estimated by reflectivity (r_{rad}) multiplied by the incident radiative heat flux (q''_{rad}) in the opposite direction against the wall, and the plotted q''_{em} is its absolute value.

The convective heat flux is estimated by

$$q''_{conv} = \lambda_{inter} \frac{T_{first} - T_{inter}}{1/2\Delta y_{wall}} \qquad \text{W/m}^2 \qquad (19)$$

The others terms are net heat flux $q''_{net}(=q''_{tot} - q''_{em})$ and total heat flux $q''_{tot}(= q''_{conv} + q''_{rad})$. q''_{rad} consists of components, i.e. (i) incident radiative heat flux owing to the combustion of the gaseous fuel $q''_{rad,gas}$ and (ii) that owing to soot $q''_{rad,soot}$. A different simulation started with the same data with $C_{soot} = 0$ (see supplemental materials [27]) removes $q''_{rad,soot}$ from q''_{rad}, extracting $q''_{rad,gas}$. Finally, $q''_{rad,soot}$ is given by $q''_{rad,soot} = q''_{rad} - q''_{rad,gas}$. Furthermore, the present study evaluates the contribution of heat flux components. q''_{conv}/q''_{tot} is the ratio of convective heat flux to total heat flux, and q''_{rad}/q''_{tot} is the ratio of incident radiative heat flux to total heat flux. $q''_{rad,gas}/q''_{rad}$ is the ratio of incident radiative heat flux due to combustion of the gaseous fuel to incident radiative heat flux, and $q''_{rad,soot}/q''_{rad}$ is the ratio of incident radiative heat flux due to soot to incident radiative heat flux.

3. Results

3.1. Medium-scale full wall fire scenarios

Several simulations of a medium-scale full wall fire scenario were performed to test a model sensitivity and support the prediction accuracy of heat fluxes presented in the following sections. Hebert et al. [20] measured the soot volume fraction on PMMA walls under the full wall fire condition; therefore, their experimental data are suitable for validation of the soot model.

3.1.1. Sensitivity test for grid resolution and radiation calculation
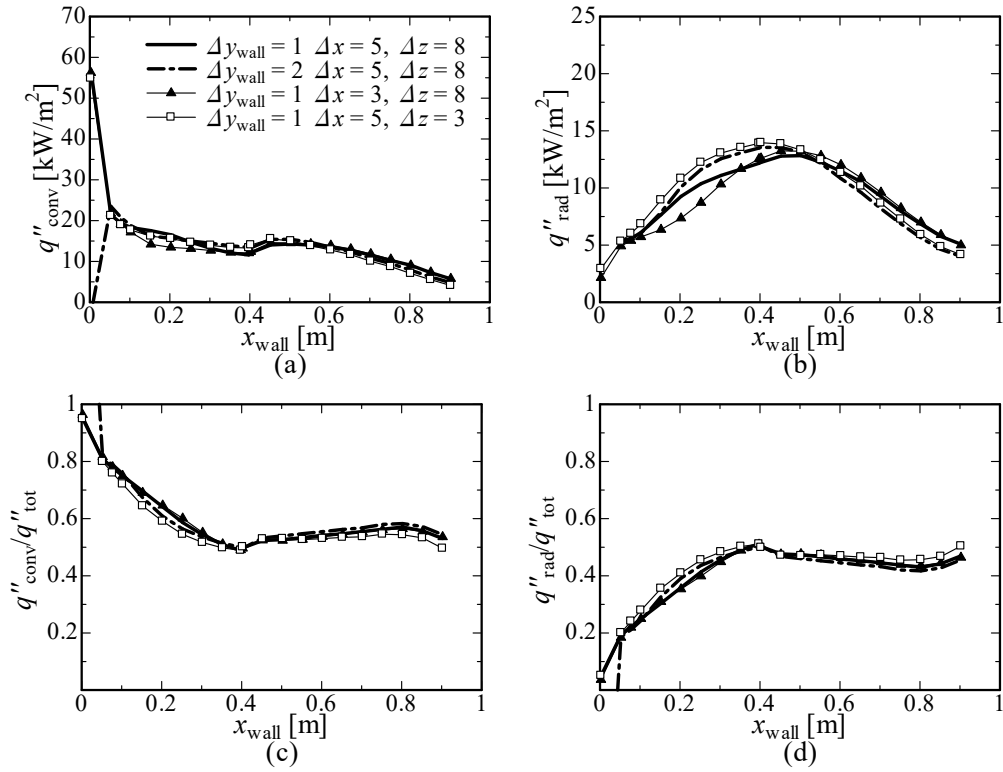
Fig. 3 Grid sensitivity test in the y-direction along the centre of the wall.

Figures 3(a) and (b) show q''_{conv} and q''_{rad} computed with the different first layer distances Δy_{wall}. The previous study used $\Delta x = 5$, $\Delta y_{wall} = 1.91$, and $\Delta z = 8$ mm [1]. However, small q''_{conv} appears at x_{wall} ≈ 0 m with $\Delta y_{wall} = 2$ mm owing to extinction here, and the present study must use $\Delta y_{wall} = 1$ mm. The aspect ratio of the first grid next to the wall becomes large because of this change, and additional tests show the slight influences of Δx and Δz in Fig. 3. Its impact exists on the pyrolysis surface ($x_{wall} > 0.4$

m) in q''_{conv} and q''_{rad}. Unfortunately, it was not easy to prepare $\Delta x = 3$, $\Delta y_{wall} = 1$, and $\Delta z = 3$ mm for

large-scale flame spread simulations owing to its high computation cost. However, the predicted

ratios at different grid resolutions are close, as shown in Fig 3(c) and (d). The present simulations

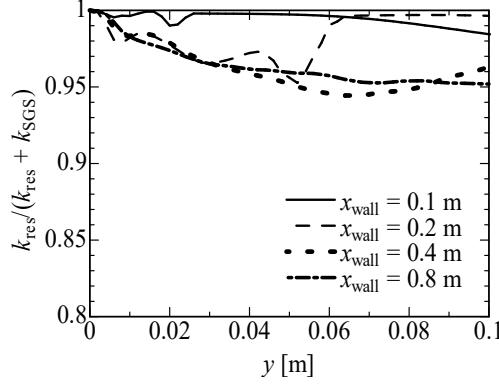employed $\Delta x = 5$, $\Delta y_{wall} = 1$, and $\Delta z = 8$ mm in the following sections.

Fig. 4 Turbulence resolution at different x_{wall}. The span wise coordinate is $z = 0$.

Maragkos et al. [22] evaluated turbulent resolution as $k_{res}/(k_{res} + k_{SGS})$, where k_{res} and k_{SGS} are the

resolved turbulence kinetic energy and sub-grid scale turbulence kinetic energy, respectively. k_{SGS} is

modelled following the authors' previous study [1], and k_{res} is obtained through post-processing:

$$k_{res} = \frac{1}{2}\mathbf{u'}^2 \qquad m^2/s^2 \tag{20}$$

where $\mathbf{u'}$ is the fluctuation of velocity vector. The mean turbulent resolution is plotted in Fig. 4. The

resolution should be > 0.8 according to Pope [39], and so the prediction sufficiently captures

turbulence with the computational grid.
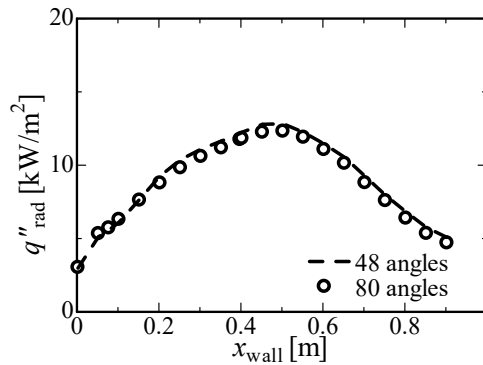
Fig. 5 Sensitivity test for the number of angles in radiation calculation along the centre of the wall.

Figure 5 shows a sensitivity test for the number of angles in the radiation solver. A minimal difference is found between 48–80 angles, and therefore, 48 angles are sufficient for this simulation.

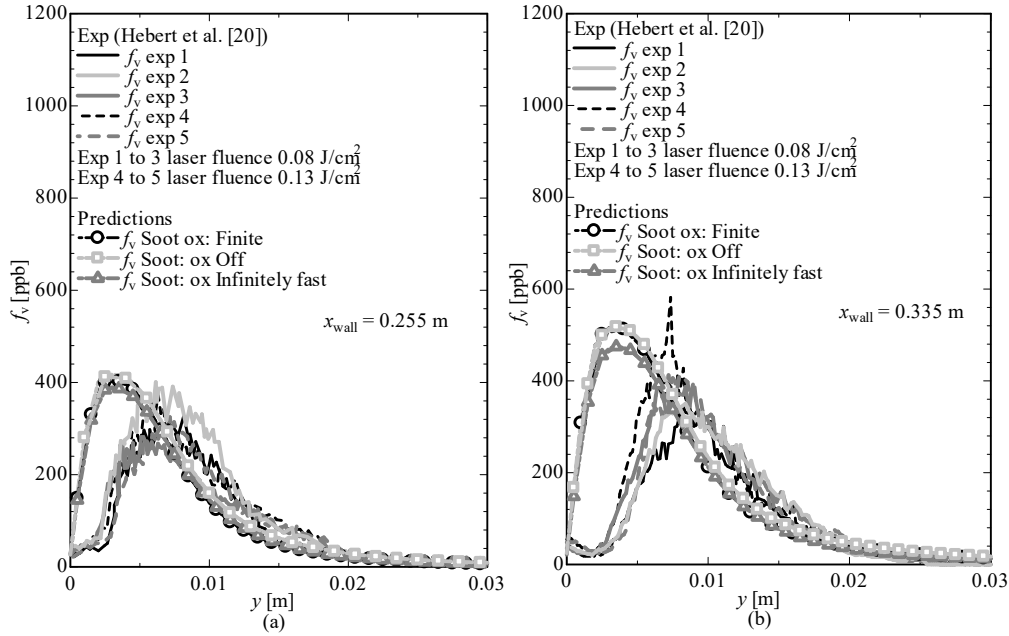### 3.1.2. Sensitivity test for the soot oxidation model

Fig. 6 Predicted soot volume fraction f_v compared with Hebert's experimental data [20].

Figure 6 compares predicted f_v with Hebert's experimental data. 'Soot ox: Finite' is finite-rate chemistry for soot oxidation model, 'Soot ox: Off' is no consideration of soot oxidation model, and 'Soot ox: Infinitely fast' is infinitely fast chemistry for soot oxidation. The present model is 'Soot ox Finite'. The predicted data are reported at 0.05 m from the side edge, just as in the experiment [20]. Since different laser fluence gave different soot volume fractions, Hebert et al. presented several ones.

The measured f_v is 260–390 ppb at $x_{wall} = 0.255$ m and $y \approx 0.0066$ m and is 270–580 ppb at $x_{wall} = 0.335$ m and $y \approx 0.0074$ m. In contrast, the predicted f_v is 410 ppb at $x_{wall} = 0.255$ m and $y \approx 0.003$ m and is 520 ppb at $x_{wall} = 0.335$ m and $y \approx 0.003$ m. The computed peak positions contain a 53–55% error, and the soot volume fractions include a 0–5% error.

From the comparison of the predictions, the influence of soot oxidation on the soot volume fraction is minimal. In contrast, the treatment of infinitely fast chemistry provides the lower soot volume fraction than that obtained by the treatment of finite-rate chemistry.

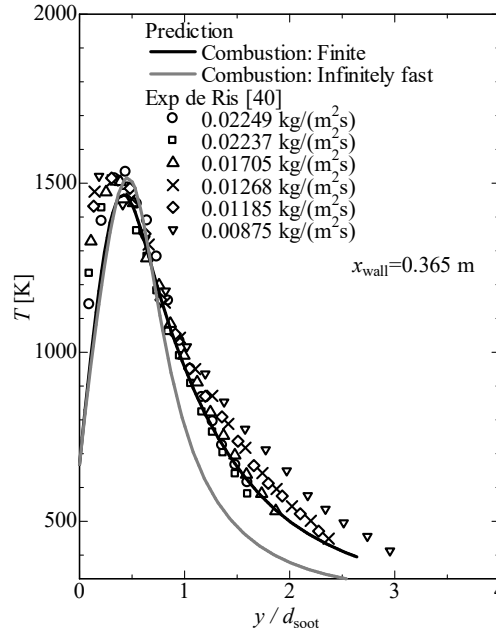### 3.1.3. Sensitivity test for the chemistry treatment

Fig. 7 Model sensitivity test for T.

In Fig. 7, the predicted temperatures are compared against the experimental data of de Ris et al. [40]. de Ris et al. plotted the temperature distribution and upward velocity against the distance from the wall scaled by the soot depth obtained from the experiment of de Ris et al. [40], where $d_{soot} = 0.0189$ m. The spanwise coordinate is $z = 0$. Many previous investigators used infinitely fast chemistry for flame spread, pool fire, and full wall fire simulations [15–17,19,21,22,26]. Nevertheless, the present prediction shows better temperature predictions after the peak when using finite-rate chemistry. This difference may cause a difference in the prediction of heat flux.
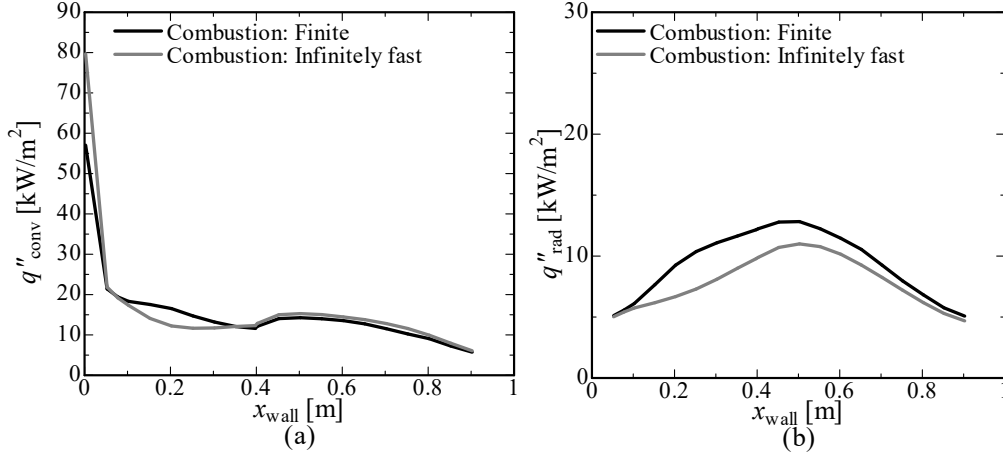
Fig. 8 Model sensitivity test for convective heat flux q''_{conv} and radiative heat flux q''_{rad} along the centre of the wall.

Figure 8 shows a model sensitivity test for q''_{conv} and q''_{rad}. Notably, finite-rate chemistry for combustion gives a 14.2% difference in the peak q''_{rad} compared with that obtained by infinitely fast chemistry, as shown in Fig. 8 (b). q''_{conv} obtained by infinitely fast chemistry is less than that obtained by finite-rate chemistry below the pyrolysis front location. Above the pyrolysis front, the treatment of the infinitely fast chemistry yields slightly higher values.

3.1.4. For medium-scale full wall fire scenarios

Figure 9 shows the total and individual heat fluxes and fractions of individual components. It is noteworthy again that the wall temperature is $T = 668$ K, which indicates that q''_{conv} is solely affected by the flame temperature. $q''_{rad,soot}$ is reasonably predicted because of the validation of f_v in Fig. 6.

The respective terms of heat flux at $x_{wall}/x_p = 1.0$ are $q''_{conv} = 11.6$ kW/m^2, $q''_{rad} = 12.2$ kW, $q''_{rad,gas}$ = 8.8 kW, and $q''_{rad,soot} = 3.3$ kW. Their fractions are $q''_{conv}/q''_{tot} = 46.3\%$, $q''_{rad}/q''_{tot} = 53.7\%$, $q''_{rad,gas}/q''_{rad} = 68.0\%$, and $q''_{rad,soot}/q''_{rad} = 32.0\%$, respectively.
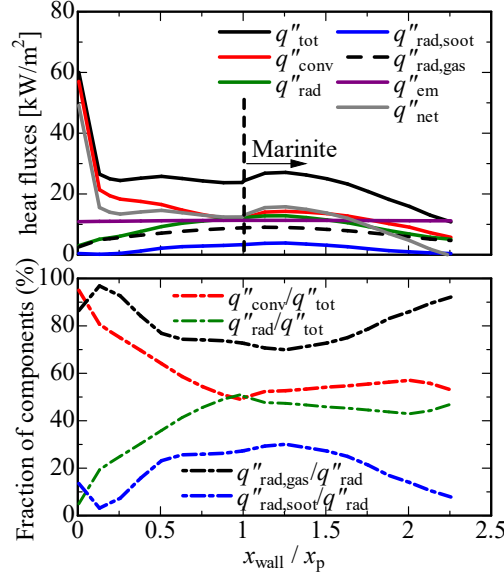
Fig. 9 Total and individual heat fluxes and fractions of individual components for Hebert et al.'s experimental scenario along the centre of the wall.
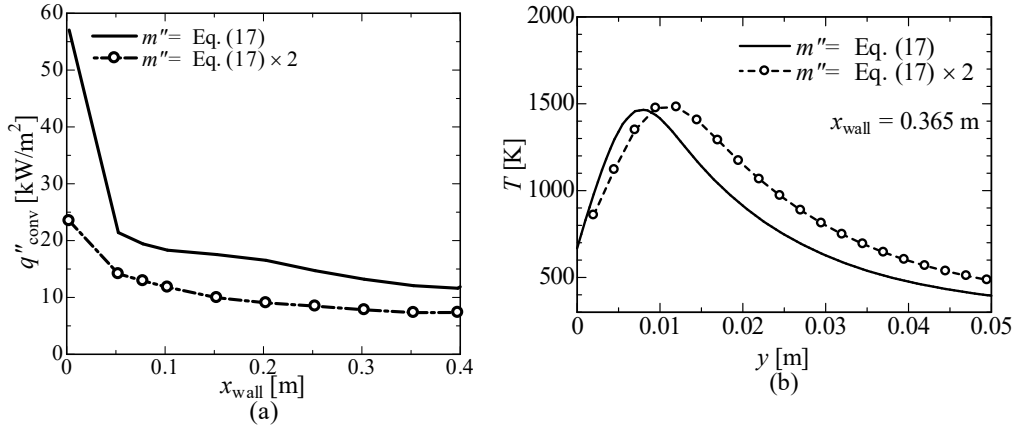
3.1.5. Blowing effect

Fig. 10 (a) Predicted convective heat flux q''_{conv} on the wall and (b) temperature in the y-direction with different mass-loss rates m''.

Figure 10(a) is the predicted q''_{conv} obtained by different mass-loss rates. The larger mass-loss rate provides the lower convective heat flux, and this phenomenon refers to 'blowing effect'. As shown in Fig. 10(b), the twice larger mass-loss rate gives the approximately 50% longer standoff distance $y_{standoff}$ than that using Eq. (17), where $y_{standoff}$ is the distance from the wall with the peak temperature. The larger pyrolysis flow opposes the direction of convective heating and thus results in cooling of

25

the surface. The estimation of q''_{conv} is $q''_{conv} = \lambda_{inter}(T_{first} - T_{inter})/(0.5\Delta y_{wall})$; thus, q''_{conv} is lower with the larger mass-loss rate.

3.2. Large-scale full wall fire scenario

Figure 11 shows the predicted q''_{tot}, q''_{conv}, and q''_{rad} compared with the experimental data of Orloff et al.'s [3] and Singh and Gollner [7]. Although the geometry size is different, these datasets are comparable owing to their similar m''. Orloff et al. used a PMMA wall with $H = 1.47$ m; therefore, the predicted data are comparable only for $0 < x_{wall} < 1.0$ m. The choice of different wall heights is to compare the predicted data later discussed in Fig. 16. The calculated q''_{conv} is close to Singh and Gollner's data at $x_{wall} < 0.06$ m. Singh and Gollner [7] reported a sudden increase in the surface regression length and its rate at the trailing edge of a PMMA slab, and they termed "the trailing edge effect". Thus, their experimental data are not plotted for $x_{wall} > 0.07$ m in Fig. 11

q''_{conv} experimentally estimated by Orloff et al. is lower than the predicted data; they estimated the convective heat flux based on the energy balance on the surface of the PMMA wall:

$$q''_{rad} + q''_{conv} = m'' h_{gas} + q''_{em}, \tag{21}$$

where $h_{gas} = 1.611 \times 10^6$ J/kg [3], m'', q''_{rad}, and q''_{em} were measured in the experiment, and q''_{em} is considered positive in Eq. (21). However, h_{gas} ranges from 1.611×10^6 to 2.15×10^6 J/kg [41], and this range leads to a change in the convective heat flux. Substituting $h_g = 2.15 \times 10^6$ into Eq. (21), the modified convective heat flux $q''_{conv,mod}$ and total heat flux $q''_{tot,mod}$ are obtained, where $q''_{tot,mod} = q''_{conv,mod} + q''_{rad}$.
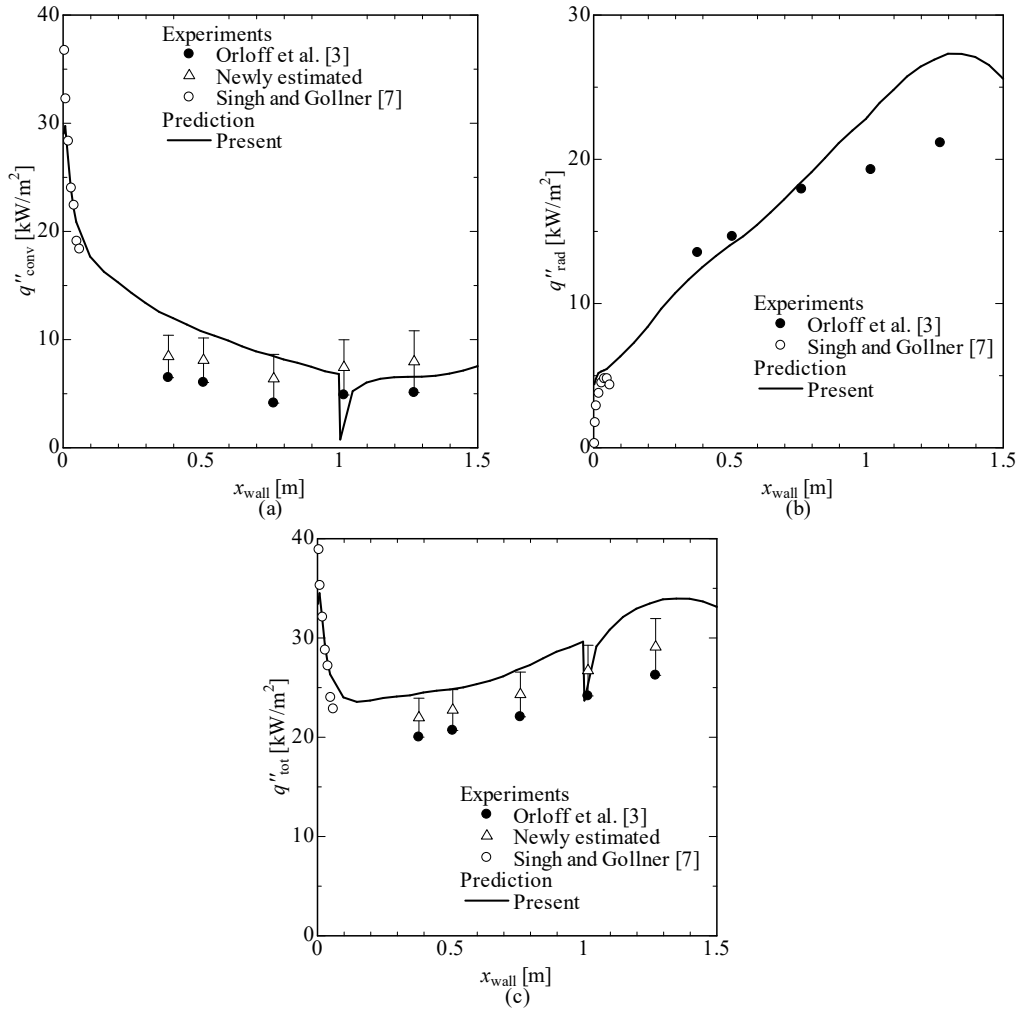
Fig. 11 Predicted total, convective, and radiative heat fluxes compared with the experimental data [3,7] along the centre of the wall. Refer to the texts for the explanation of 'Newly estimated' experimental values.

Table 1 Errors of convective, radiative, and total heat fluxes.

x_{wall}	error of q''_{conv}	error of q''_{rad}	error of q''_{tot}
0.06 m	9.3%	30.6%	12.7%
0.381 m	17.0%	-9,6%	2%
0.508 m	5.5%	-3.4%	0.2%
0.762 m	0%	2.9%	1.3%
1.0 m	0%	18.3%	1.2%

Figure 11 compares the predictions of q''_{conv}, q''_{rad}, and q''_{tot} with the experimental data. Figure 11 labels $q''_{conv,mod}$–q''_{conv} [3] and $q''_{tot,mod}$–q''_{tot} [3] 'Newly estimated'. Table. 1 lists errors of convective, radiative, and total heat fluxes. The error estimations of convective and total heat fluxes are based on the comparison of Singh and Gollner's data [7] and the range of 'Newly estimated'. For example, the upper bound of the newly estimated q''_{conv} at x_{wall} = 0.381 m is 10.403 kW/m^2, and the predicted q''_{conv} is 12.175 kW/m^2. The error of q''_{conv} at x_{wall} = 0.381 m is estimated as Err = (12.175 – 10.403)/12.175 × 100 = 17.036%.

Furthermore, that of radiative heat flux is based on Singh and Gollner's data and Orloff et al.'s data [3]. The errors are relatively large at x_{wall} = 0.06 m because heat fluxes changes sharply near here. For $x_{wall} \geq$ 0.381 m, the errors are small, except for the error of q''_{conv} at x_{wall} = 0.381 m and that of q''_{rad} at x_{wall} = 1 m. The present model estimates h_{gas} as

$$h_{gas} = h_{vap} + h_{mel} + h_p + Cp_{solid}(T_p - 293) \approx 2.03 \times 10^6 \quad \text{J/kg,} \tag{22}$$

where the pyrolysis temperature T_p = 580 K [1], the vaporisation heat h_{vap} = 3.6 × 10^5 J/kg [1], the melting heat h_{mel} = 1.8 × 10^5 J/kg [1], the pyrolysis heat h_p = 8.4 × 10^5 J/kg [1], and the mean Cp_{solid} = 2270 J/kg/K [1]. Since h_{gas} in the present model is close to that of Wilde [41], the predicted q''_{conv} and q''_{tot} should match the upper bound heat fluxes.

As shown in Fig. 11, the predicted q''_{rad} values are slightly lower at x_{wall} = 0.4 than the experimental values and is slightly higher at x_{wall} = 1.0 m. f_v is a small value; it is difficult to calculate an accurate value quantitatively, ranging from 250 to 450 ppb at x_{wall} = 0.255 and 0.335 m in Hebert et al.'s experiment [20]. The absorption coefficient of soot $a_{rad,S}$ is computed as $a_{rad,S}$ = 1862$f_v T$ [1]; hence f_v directly influences a_S. The previous experiments did not provide sufficient soot data. Thus, soot is not generally taken into account or not validated even though the soot concentration influences radiation calculation [8–12,21].
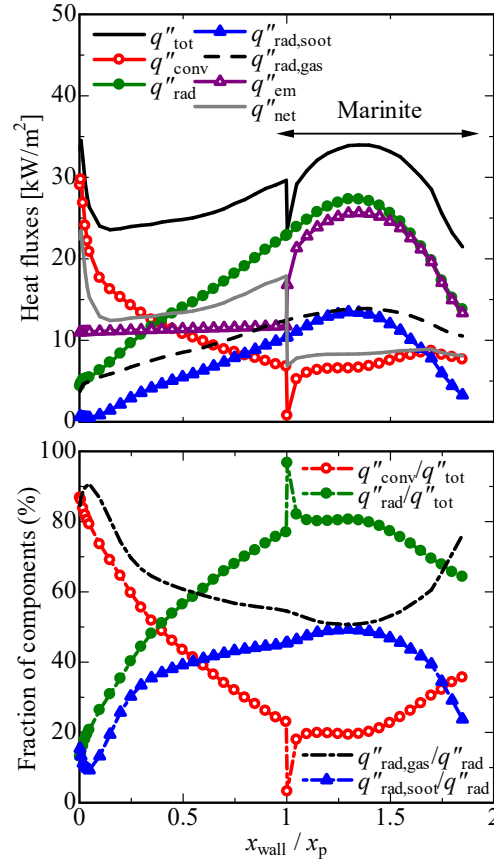
Fig. 12 Total and individual heat fluxes and fractions of individual components for large-scale full wall fire scenario along the centre of the wall.

Figure 12 shows the total and individual heat fluxes and fractions of individual components for large-scale full wall fire scenario.

Orloff et al. suggested [3] that q''_{rad}/q''_{tot} is 75–80% at $x_{wall} > 0.76$ m, whereas in the present study, that is approximately 70%.

The convective heat flux decreases by 88.7% at $x_{wall}/x_p = 1$ because of a sudden rise in the surface temperature with no pyrolysis on the marinate wall (note that a higher surface temperature causes the lower temperature gradient between the hot combustion gases and the surface). This discontinuity disappears further above the pyrolysis front because the surface temperatures drop.

The respective terms of heat flux just before $x_{wall}/x_p = 1.0$ are $q''_{conv} = 6.8$ kW/m^2, $q''_{rad} = 22.8$ kW/m^2, $q''_{rad,gas} = 12.4$ kW/m^2, and $q''_{rad,soot} = 10.4$ kW/m^2. Their fractions are $q''_{conv}/q''_{tot} = 23.0\%$, $q''_{rad}/q''_{tot} = 77.0\%$, $q''_{rad,gas}/q''_{rad} = 54.6\%$, and $q''_{rad,soot}/q''_{rad} = 45.4\%$, respectively. By scale-up of the

29

PMMA size from 0.4 to 1.0 m, q''_{conv} decreases by 41.4%; q''_{rad}, $q''_{rad,gas}$, and $q''_{rad,soot}$ increases by 86.9%, 40.9%, and 215.2%, respectively.

3.3. Large-scale upward flame spread scenario

3.3.1. Validation

The present sections simulated the flame spread tests of Liang et al. [6] over a 1 m PMMA slab, considering the non-combustible wall region. Note that the shape of the pyrolysis front is non-uniform in principle, but all the data is monitored only at $z = 0$ m.

Figure 13 shows an overview of flame spread on the PMMA wall visualised by the flame volume. Yang et al. [42] defined it by the following equation in respective cells:

$$R_0 = \frac{1}{1 + s\tilde{Y}_{fu}/\tilde{Y}_{O_2}},$$ (23)

where the inside of the flame is for $0 \le R_0 \le 0.99$. Our previous study [1] showed that the above criterion agreed with the predicted x_f, and thus it is useful for the purpose of visualising the fire growth. In Fig. 13, CF is the continuous flame region; IF, the intermittent flame region; PL, the plume region; LR, the laminar region; L-T, the laminar-turbulence transition region; and TR is the turbulence region. For clarity, Fig. 13 marks three different regions in the turbulent non-premixed flame when x_p = 0.5 m using the dimensionless parameter defined by Consalvi et al. [8]:

$$\xi = (x_{wall} - x_p)/(x_f - x_p),$$ (24)

where CF corresponds to $\xi < 0.4$, IF to $0.4 \le \xi \le 1.6$, and PL to $\xi > 1.6$.
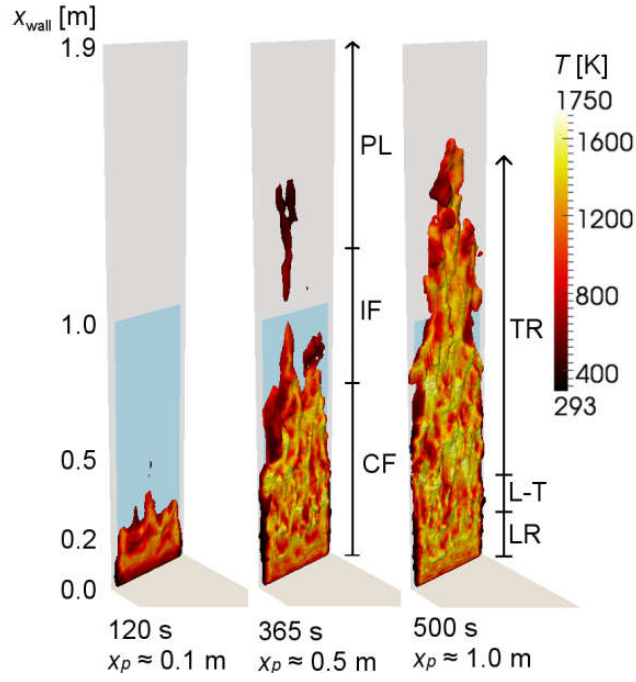
Fig. 13 Snapshots of flame spread when $x_p = 0.1$, 0.5 and 1.0 m. The animation file of flame spread can be found in supplemental materials [27].

According to previous studies [1,3], the laminar region was until $x_{wall} \approx 0.18$ m [3]. At $x_{wall} \approx 0.3$ m, the flame is almost at the end of the laminar-turbulent transition region and $x_{wall} \approx 0.6$ m, the flame is already fully turbulent. The predictions suggest that the laminar region (LR) is $0 < x_{wall} < 0.18$ m, laminar-turbulent transition region (L-T) is 0.18 m $< x_{wall} < 0.3$ m and the turbulent region (TR) is 0.3 m $< x_{wall}$, as denoted on the flame volume for $x_p = 1.0$ m in Fig. 13.
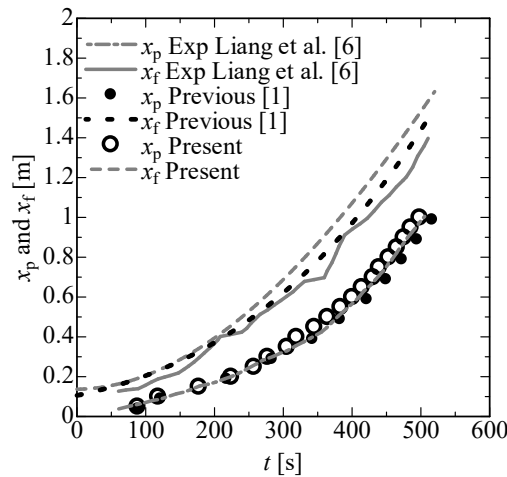

Fig. 14 Flame height (x_f) and pyrolysis height (x_p) versus time. The predicted x_p is taken at the centre of the wall. The animation of the progress of pyrolysis front can be found in supplemental materials [27].

Figure 14 depicts the computed and experimental pyrolysis height x_p and flame height x_f versus time from the ignition, where $x_f = \max(x - x_a)$ when $\tilde{Y}_{fu} - \tilde{Y}_{O_2} / s \geq 0$, where max() indicates the maximum coordinate [43]. Although the predicted pyrolysis height seems to be in reasonable agreement with the measurement, the predicted flame height is slightly over-predicted. In experiments, the definition of flame height is dependent on the intermittency and final burn-out of a luminous flame [43]. Liang et al.'s experiment [6] determined the flame height using recoded flame images, and there is not a unique definition. This fact leads to the difficulty of quantitative agreement between simulation and experiment. The global errors evaluated based on a standard deviation [27,44] of x_p and x_f are 2.7% and 9.0%.

3.3.2. Analysis of heat flux components and soot influences

This section analyses the heat flux components and influences of soot. The average duration was 10 s started from particular pyrolysis times (t = 120, 275, 365, 430, and 500 s). These times approximately corresponds for x_p = 0.1, 0.3 0.5, 0.7, and 1.0 m. However, it is not easy to get the average data of unsteady phenomena, such as flame spreading.
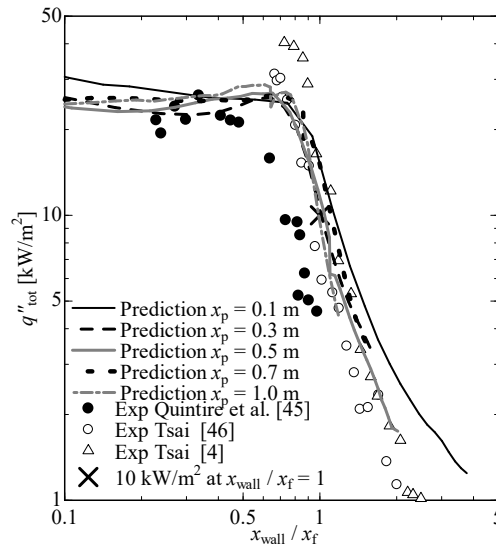

Fig. 15 Total heat flux q''_{tot} vs x_{wall}/x_f for validation.

This analysis needs the average heat fluxes at the respective times and so uses the mass-loss rate and wall temperature obtained from the above times as the velocity and temperature inlet conditions. The analysis used the fixed mass-loss rates obtained from the respective times because these values change for 10 s. Also, the wall temperature increases during the averaging process, reducing q''_{conv}. It is desirable to use the wall temperature at the respective times as close as possible. Therefore, the present analysis reset this increase in the wall temperature for 10 s to keep the initial temperatures at the respective times. Using this modified wall temperature provides a better estimate for q''_{conv} at the respective times. A reason behind the fixed wall temperature was not used was that a change in the wall temperature distribution was prominent per time step. If the averaging time is longer than that of the present study (= 10 s), the discrepancy would be more significant.

Quintiere et al. [45] reported the total heat flux on several materials such as particleboard, aircraft panel, flexible foam, carpet panel, rigid foam and PMMA panel. They found the logarithmic association between q''_{tot} and x_{wall}/x_f, which is applicable for not only PMMA but also other materials. In Fig. 15, the calculated q''_{tot} is close to that of Tsai's experimental data [46] at $1 < x_{wall}/x_f$. q''_{tot} at the flame tip ($x_{wall}/x_f = 1.0$) is 10 kW/m^2. It is noteworthy that the experimental evolution profiles are slightly different, although the same material was used in the experiments [4,46]. The definition of x_f affects the profiles, but the magnitude of q''_{tot} is dependent on those of q''_{conv} and q''_{rad}. A possible explanation for a difference in q''_{tot} is a variation in Δh_{comb} of the PMMA material, which ranges from 2.42×10^7 [6] to 2.68×10^7 J/kg [47].

Figure 16 shows the total and individual heat flux components and their fractions when $x_p \approx 0.1, 0.3, 0.5, 0.7,$ and 1.0 m; also plots the heat fluxes for the non-combustible wall region when $x_p \approx 0.5, 0.7,$ and 1.0 m. A transient heat flux change is also presented in supplemental materials [27]. Notably, a sudden rise of wall temperature with no pyrolysis at $x_{wall} = 1.0$ m causes a sudden shift in convective and re-radiative heat fluxes. The convective heat flux decreases by 33.7–36.3%, and re-radiative heat flux increases by 48.1–103.2% when $x_p = 0.5$–1.0 m.

33

When $x_p \approx 0.1$ m, a flame is laminar at $x_{wall} < 0.18$ m as discussed above; therefore, the entire region is laminar. q''_{tot} and q''_{conv} decrease sharply with an increase in x_{wall} near the bottom leading edge owing to the relatively high gas temperature there [1,7], then the rate of decrease slows down until $x_{wall}/x_p \approx 2$; afterwards q''_{tot}, q''_{conv} and q''_{net} start to decrease rapidly shortly after the start of the intermittent flame region at $x_{wall}/x_p \approx 1.65$. Near the bottom leading edge of the PMMA, q''_{tot}, q''_{net} and q''_{re} are very high because of high q''_{conv}. q''_{conv}/q''_{tot} is approximately 80%; q''_{rad}/q''_{tot} is approximately 20%. These values are quantitatively in line with the measurements of Singh and Gollner [7].

Evolution trends of the total and individual heat fluxes when x_p reaches 0.3, 0.5, 0.7, and 1.0 m are similar. A flame is under transient–fully turbulent state based on the author's previous study [1]. q''_{tot}, q''_{conv}, q''_{re}, and q''_{net} decrease sharply with an increase in x_{wall} near the bottom leading edge of the PMMA. All the individual heat fluxes gradually grow in the continuous flame region and start to decrease near the end of the continuous flame region.

As a flame spreads upward, q''_{conv} decreases and q''_{rad} increases. When $x_p = 0.3$ m, $q''_{conv} \approx 15.7$ kW/m^2, $q''_{rad} \approx 8.6$ kW/m^2, $q''_{rad,gas} \approx 6.8$ kW/m^2, and $q''_{rad,soot} \approx 1.8$ kW/m^2 at the location of the pyrolysis front ($x_{wall}/x_p \approx 1.0$). Also, when $x_p = 1.0$ m, those change to $q''_{conv} \approx 11.5$ kW/m^2, $q''_{rad} \approx 16.7$ kW/m^2, $q''_{rad,gas} \approx 10.7$ kW/m^2, and $q''_{rad,soot} \approx 6.0$ kW/m^2, respectively. Namely, q''_{conv} decreases by 26.8%, and q''_{rad}, $q''_{rad,gas}$, and $q''_{rad,soot}$ rise by 94.2%, 55.9%, and 233.3% between $x_p = 0.3$–1.0 m.

A decrease in q''_{conv} with flame spreading is due to an increase in the standoff distance. Decreasing q''_{conv} at a higher x_{wall} could be confirmed in reference [7]. q''_{rad} increases with flame spreading. The predicted f_v at the pyrolysis front rises with progress in x_p, as shown in Fig. 17(a), and thus the contribution of $q''_{rad,soot}$ on heat transfer increases. Conversely, the peak of the mass fractions of products remains almost constant at different x_p, but the mass fraction diffuses toward the outer region (y-direction) more and more at higher heights, as shown in Fig. 17(b). Therefore, $q''_{rad,gas}$ slightly

increases as fire growth. A tendency for $q''_{rad,gas}/q''_{rad}$ and q''_{conv}/q''_{tot} are similar because combustion products and temperature influence $q''_{rad,gas}$ and q''_{conv} .

Regardless of the progress of flame spread, q''_{rad}/q''_{tot} increases, and q''_{conv}/q''_{tot} decreases in the continuous flame region. In the intermittent flame and plume regions, q''_{rad}/q''_{tot} decreases and q''_{conv}/q''_{tot} increases i.e. q''_{conv} becomes dominant after the continuous flame region.
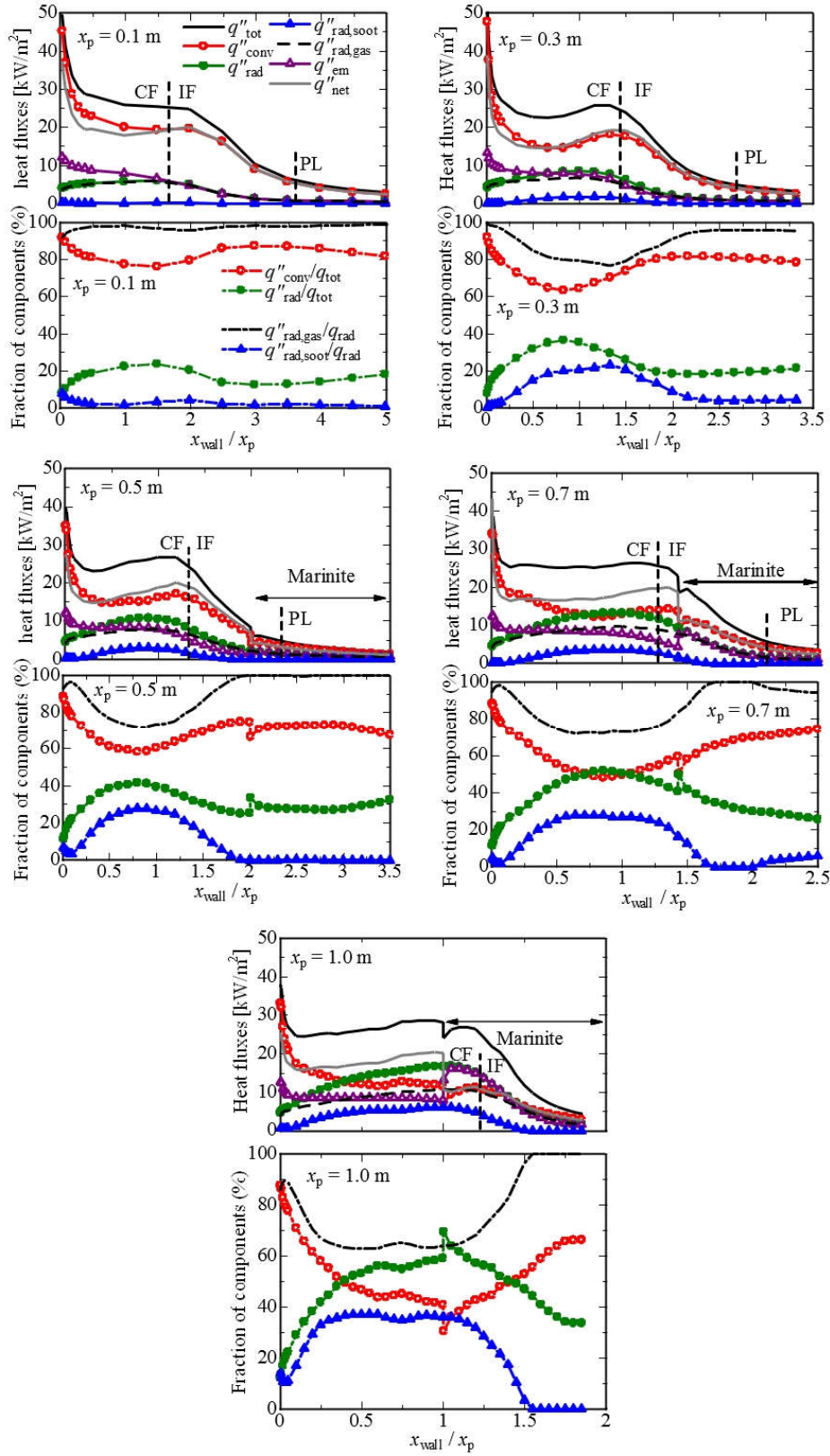
Fig. 16 Total and individual heat fluxes and fractions of individual components at $x_p \approx 0.1$–1.0 m (The border of the continuous flame (CF) and intermittent flame (IF) is also depicted). The data are taken at the centre of the wall. Transient heat flux evolution is also presented in supplemental materials [27].
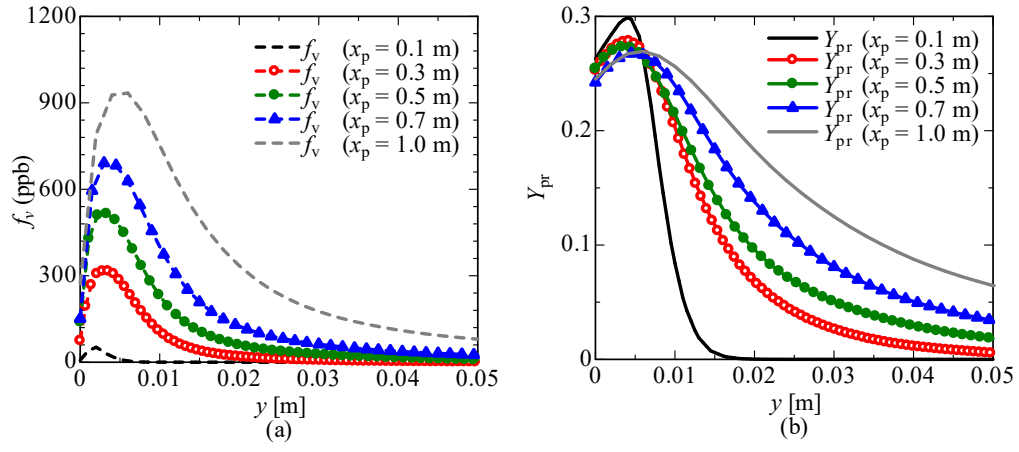
Fig. 17 (a) Variation of soot volume fraction f_v (left) and (b) the mass fraction of products (right) with the distance from the wall at the location of the pyrolysis front, where $Y_{pr} = Y_{H2O}+Y_{CO2}$.
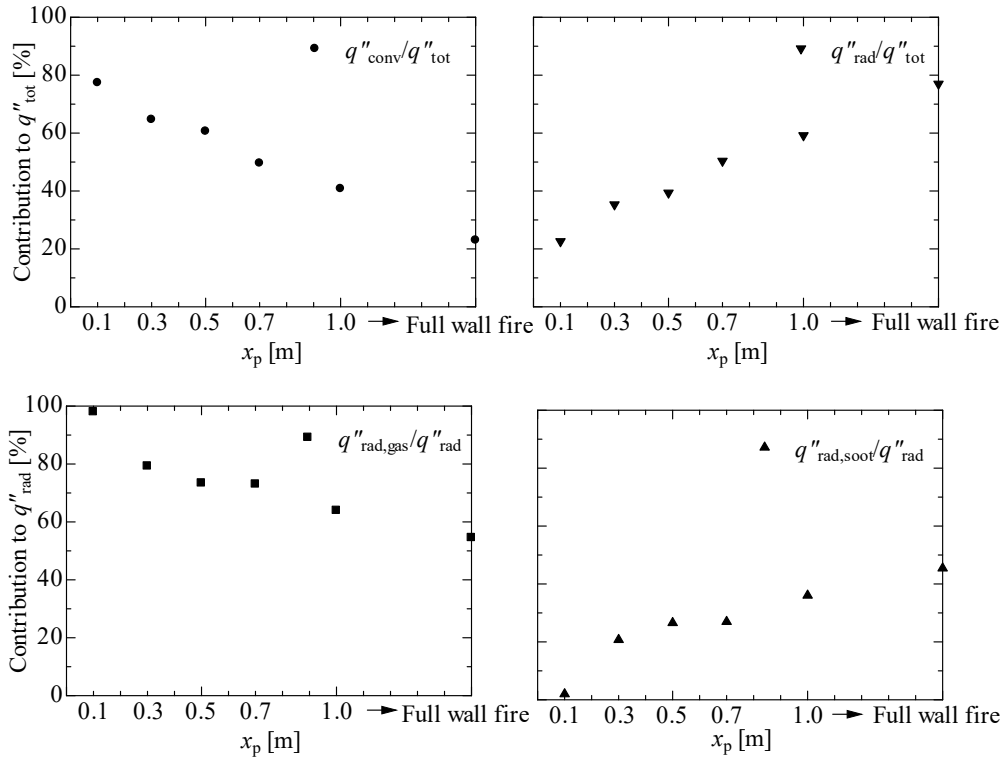

Fig. 18 Contributions to q''_{tot} of q''_{conv} and q''_{rad}, as well as contributions to q''_{rad} of $q''_{rad,gas}$ and $q''_{rad,soot}$ at the location of the pyrolysis front as it advances upward.

In summary, figures 18 and 19 show the contributions to q''_{tot} of q''_{conv}, q''_{rad} and $q''_{rad,soot}$ *vs* flame spread conditions. The predictions under the full wall fire condition are obtained from Fig. 11.

In Fig. 18, at the location of the pyrolysis front, $q''_{conv}/q''_{tot} \approx 64.7\%$ and $q''_{rad}/q''_{tot} \approx 35.3\%$ when $x_p \approx 0.3$ m. $q''_{conv}/q''_{tot} \approx 40.8\%$ and $q''_{rad}/q''_{tot} \approx 59.2\%$ when $x_p \approx 1.0$ m. $q''_{conv}/q''_{tot} \approx 23.0\%$ and $q''_{rad}/q''_{tot} \approx 77.0\%$ in the full wall fire scenario. In Fig. 19, at the position of flame height, $q''_{conv}/q''_{tot} \approx 81.5\%$ and $q''_{rad}/q''_{tot} \approx 18.5\%$ when $x_p \approx 0.3$ m. $q''_{conv}/q''_{tot} \approx 55.8\%$ and $q''_{rad}/q''_{tot} \approx 44.2\%$ when $x_p \approx 1.0$ m. $q''_{conv}/q''_{tot} \approx 55.8\%$ and $q''_{rad}/q''_{tot} \approx 44.2\%$ in the full wall fire scenario.

As a flame spread upward, the impact of radiation on heat transfer becomes large. At the coordinate of the pyrolysis front, q''_{conv}/q''_{tot} decreases by 37.0%, and q''_{rad}/q''_{tot} increases by 67.7% between $x_p = 0.3$–1.0 m. At the coordinate of the flame height, q''_{conv}/q''_{tot} decreases by 31.5%, and q''_{rad}/q''_{tot} increases by 139.0%.

At the location of the pyrolysis front, $q''_{rad,soot}/q''_{rad} \approx 20.7\%$ when $x_p \approx 0.3$ m, and $q''_{rad,soot}/q''_{rad} \approx 36.0\%$ when $x_p \approx 1.0$ m. Under the full wall fire condition, $q''_{rad,soot}/q''_{rad} \approx 45.4\%$. From $x_p \approx 0.3$–1.0 m, $q''_{rad,soot}/q''_{rad}$ increases by 73.9%. Furthermore, at the coordinate of the flame height, $q''_{rad,soot}/q''_{rad} \approx 8.0\%$ when $x_p \approx 0.3$ m, and $q''_{rad,soot}/q''_{rad} \approx 0\%$ when $x_p \approx 1.0$ m.

As the flames spread upward, the contribution of soot to radiation becomes more and more important at the location of the pyrolysis front. However, at the position of the flame height, the contribution of $q''_{rad,soot}$ is minor and disappears when $x_p \approx 1.0$ m. In other words, at the location of the pyrolysis front, soot played an important role, whereas, at the position of the flame height, the soot concentration did not influence heat transfer.
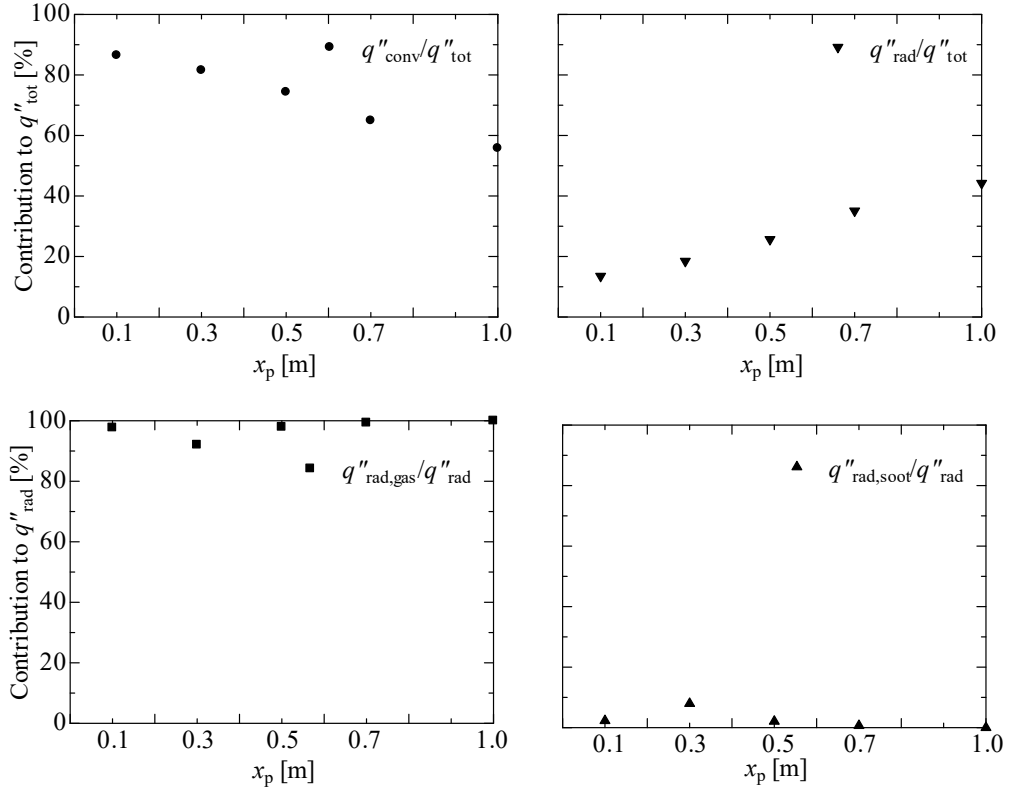
Fig. 19 Contributions to q''_{tot} of q''_{conv}, q''_{rad}, as well as contributions to q''_{rad} of $q''_{rad,gas}$ and $q''_{rad,soot}$ at the location of the flame tip as it advances upward.
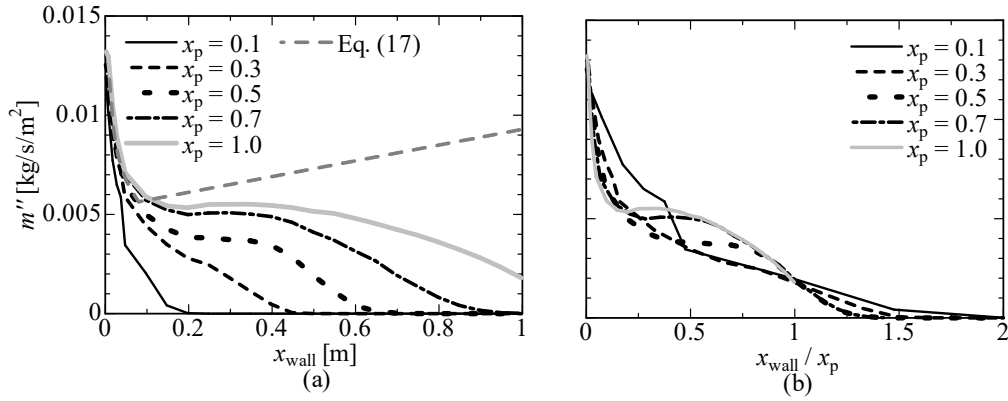

Fig. 20 (a) Mass-loss rate m'' vs x_{wall} for the flame spread (x_p = 0.1–1.0 m) and full wall fire state (Eq. (17)). (b) Corresponding m'' for the flame spread scenario. These data is taken along the centre of the wall.

Figure 20 shows the predicted mass-loss rate for the flame spread versus that for the full wall fire states. The distribution is larger from that under the full wall fire condition, as shown in Fig.20(a). The increasing mass-loss rate gives the decreasing convective heat flux, termed the blowing effect (see

Section 3.1.5). This increase in the mass-loss rate grows the soot volume fraction. For example, Fig. 6 showed 410 ppb at x_{wall} = 0.255 m and 520 ppb at x_{wall} = 0.335 m. Conversely, Fig. 17 illustrates approximately 320 ppb. The predicted $q''_{rad,soot}$ increases because of an increase in f_v. When the distribution of the mass-loss rate is close, a trend in the heat flux would be similar. For instance, the heat flux distributions are similar when x_p = 0.7 and 1.0 m because of the agreement of their mass-loss rates, as shown in Fig. 20(b).

4. Conclusions

The present study analysed individual heat fluxes and soot effects on flame spread over PMMA walls using a 3-D fluid-solid coupled fire spread model based on customised FireFOAM 2.2.x. The intended tests were the medium–large scale full wall fire and large-scale flame spread configurations. We drew the following conclusions:

- ✓ Under the full wall fire state, enlarging the PMMA size from 0.4 to 1.0 m decreased q''_{conv}/q''_{tot} from 46.3 to 23.0%. It also increased q''_{conv}/q''_{tot} from 53.7 to 77.0% at the location of the pyrolysis front. Also, $q''_{rad,gas}/q''_{tot}$ decreased from 68.0 to 54.6%, and $q''_{rad,soot}/q''_{tot}$ increased from 32.0% to 45.4%.

- ✓ In the upward flame spread scenario, the impact of radiative heat transfer became significant. At the coordinate of the pyrolysis front, q''_{conv}/q''_{tot} decreased from 64.7 to 40.8% between x_p = 0.3–1.0 m. Moreover, q''_{rad}/q''_{tot} increased from 35.3 to 59.2%.

- ✓ At the location of the pyrolysis front, $q''_{rad,soot}/q''_{rad}$ increased from 20.7 to 36.0% between $x_p \approx$ 0.3–1.0 m. $q''_{rad,soot}/q''_{rad}$ was higher at a higher pyrolysis height. In contrast, at the position of the flame height, $q''_{rad,soot}/q''_{rad}$ decreased from 8.0 to 0% between $x_p \approx$ 0.3–1.0 m. Therefore, the contribution of soot to radiation is the highest near the paralysis front, while its contribution decreases further away, disappearing near the flame tip.

The present results have shed light on the role of the individual component of convective and radiative heat transfer fluxes owing to soot and gas combustion products. Precise predictions of the fire spread phenomena will hence be dependent on the sound predictions of these individual components.

Appendix

The readers can find a document about flame spread modelling and associated animation files from https://doi.org/10.17632/drtddfyvzc.1

References

[1] Fukumoto K, Wang CJ, Wen JX. Large eddy simulation of upward flame spread on PMMA walls with a fully coupled fluid-solid approach. Combust. Flame 2018;190:365–387.

[2] Drysdale D, Flame spread on inclined surfaces. Fire Safety J. 1992;18:245–254.

[3] Orloff L, de Ris J, Markstein GH. Upward turbulent fire spread and burning of fuel surface. Proc. Combust. Inst. 1975;15:183–192.

[4] Tsai KC. Influence of sidewalls on width effects of upward flame spread. Fire Safety J. 2011;46:294–304.

[5] Hasemi Y. Experimental wall flame heat transfer correlations for the analysis of upward wall flame spread, Fire Sci. Technol. 1984;4:75–90.

[6] Liang C, Cheng X, Yang H, Zhang H, Yuen KK, Experimental study of vertically upward flame spread over polymethyl methacrylate slabs at different altitudes. Fire Mater. 2016;40:472–481.

[7] Singh AV, Gollner MJ, Experimental methodology for estimation of local heat fluxes and burning rates in steady laminar boundary layer diffusion flames. Combust. Flame 2015;162:2214–2230.

[8] Consalvi JL, Pizzo Y, Porterie B. Numerical analysis of the heating process in upward flame spread over thick slabs. Fire Safety J. 2008;43:351–362.

[9] Karpov A, Shaklein A, Korepanov M, Galat A, Numerical Study of the Radiative and Turbulent Heat Flux Behavior of Upward Flame Spread Over PMMA. Fire Sci. Technol. 2017;841–848.

[10] Zeinali D. Gupta A. Maragkos G. Agarwal G. Beji T. Chaos M. Wang Y. Degroote J. Merci B. Study of the importance of non-uniform mass density in numerical simulations of fire spread over MDF panels in a corner configuration. Combust. Flame 2019;200:303–315.

[11] Liao YTT, T'ien JS. A numerical simulation of transient ignition and ignition limit of a composite solid by a localised radiant source. Combust. Theor. Model 2013;17:1096–1124.

[12] Zhao X, T'ien JS, A three-dimensional transient model for flame growth and extinction in concurrent flows. Combust. Flame 2015;162:1829–1839.

[13] FM Global, FireFOAM 2.2.x, https://github.com/fireFoam-dev/fireFoam-2.2.x (accessed on 07/Jun/2019)

[14] OpenFOAM Ltd., OpenFOAM, Source code and documentations are available from: http://www.openfoam.com/ (accessed on 07/Jun/2019)

[15] Chen Z, Wen J, Xu B, Dembele S, Extension of the eddy dissipation concept and smoke point soot model to the LES frame for fire simulations. Fire Saf. J 2014;64:12–26.

[16] Chen Z, Wen J, Xu B, Dembele S. Large eddy simulation of a medium-scale methanol pool fire using the extended eddy dissipation concept. Int. J. Heat Mass Trans. 2014;70:389–408.

[17] Wang CJ, Wen JX, Chen ZB. Simulation of large-scale LNG pool fires using FireFoam. Combust. Sci. Technol. 2014;186:1632–1649.

[18] Pizzo Y, Lallemand C, Kacem A, Kaiss A, Gerardin J, Acem A, Boulet P, Porterie B. Steady and transient pyrolysis of thick clear PMMA slab. Combust. Flame 2015;162:226–236.

[19] Huang X, Gollner MJ. Correlations for evaluation of flame spread over an inclined fuel surface. Fire safety science-proceedings of the eleventh international symposium 2014:222–233.

[20] Hebert D, Coppalle A, Talbaut M. 2D soot concentration and burning rate of a vertical PMMA slab using Laser-Induced Incandescence. Proc. Combust. Inst. 2013;34:2575–2582.

[21] Ren N, Wang Y, Vilfayeau S, Trouvé A. Large eddy simulation of vertical turbulent wall fires, Combust. Flame 2016;169:194–208.

[22] Maragkos G, Beji T, Merci B. Advances in modelling in CFD simulations of turbulent gaseous pool fires 2017;181:22–38.

[23] Nicoud F, Ducros D, Subgrid-scale stress modelling based on the square of the velocity gradient tensor. Flow Turbul. Combust. 1999;62:183–200.

[24] Fernández-Tarrazo E, Sánchez AL, Liñán A, Williams FA. A simple one-step chemistry model for partially premixed hydrocarbon combustion. Combust. Flame 2006;147:32–38.

[25] Smith TF, Shen ZF, Frledman JN. Evaluation of coefficients for the weighted sum of gray gases model. J. Heat Trans. 1982;104:602–608.

[26] Wang CJ, Liu HR, Wen JX. An improved PaSR-based soot model for turbulent fires. Appl. Therm. Eng. 2018;129:1435–1446.

[27] K. Fukumoto, C. J. Wang, J. X Wen, Supplemental materials for 'Study on the role of soot and heat fluxes in upward flame spread using a wall resolved large eddy simulation approach', https://doi.org/10.17632/drtddfyvzc.1   (accessed on 21/Sep/2019)

[28] Poling BE, Prausnitz JM, O'Connel JP. The properties of gases and liquids. 5th ed. U.S.:McGraw-Hill;2001.

[29] Burcat A. Thermochemical species in polynomial form, https://burcat.technion.ac.il/dir/ [accessed on 3th Apr. 2019]

[30] Fukumoto K, Wang CJ, Wen JX. Large eddy simulation of a syngas jet flame: effect of preferential diffusion and detailed reaction mechanism, Energ. Fuel. 2019;33:5561-5581.

[31] Gran IR, Magnussen BF. A numerical study of a bluff-body stabilized diffusion flame. Part 2. Influence of combustion modeling and finite-rate chemistry. Combust. Sci. Technol. 1996 ;119:191–217.

[32] Yao W, Zhang J, Nadjai A, Beji T, Delichatsios MA. A global soot model developed for fires: Validation in laminar flames and application in turbulent pool fires. Fire Safety J 2011;46:371–387.

[33] Lee KB, Thring MW, Beér JM. On the rate of combustion of soot in a laminar soot flame, Combust. Flame 1962;6:137–145.

[34] Leung KM, Lindstedt RP, Jones WP. A simplified reaction mechanism for soot formation in nonpremixed flames. Combust. Flame 1991;87:289–305.

[35] Chaos M, Khan MM, Krishnamoorthy N. de Ris JL, Dorofeev SB, Evaluation of optimization schemes and determination of solid fuel properties for CFD fire models using bench-scale pyrolysis tests. Proc. Combust. Inst. 2011;33:2599–2606.

[36] Staggs J. The effects of gas-phase and in-depth radiation absorption on ignition and steady burning rate of PMMA. Combust Flame 2014;161:3229–3236.

[37] Beard AN, Flashover and boundary properties. Fire Safety J. 2010;45:116–121.

[38] Orloff L, Modak AT, Alpert RL, Burning of large-scale vertical surface, Symp. (Int.) on Combust. 1977;16:1.

[39] Pope SB. Ten questions concerning the large-eddy simulation of turbulent flows. New J. Phys. 2004;6:1–24.

[40] de Ris JL, Markstein GH, Orloff L, Beaulieu PA, Similarity of turbulent wall fires. Fire Safety Sci. 2003;7:259–270.

[41] J.P. de Wilde, The heat of gasification of polyethylene and polymethylmethacrylate, Memorandum M-593, Report PML 1988 C42, SFCC Publication No. 53, Delft University of Technology, 1988.

[42] Yang W, Wlodzimierz B. Numerical study of fuel temperature influence on single gas jet combustion in highly preheated and oxygen deficient air. Energy 2005; 30:385–398.

[43] Wang Y, Chatterjee P, de Ris J.L, Large eddy simulation of fire plumes, Proc. Combust. Inst. 2011;33:2473–2480.

[44] Fukumoto K, Ogami Y, Turbulent diffusion combustion model using chemical equilibrium combined with the eddy dissipation concept for reducing detailed chemical mechanisms: An application of H_2-air turbulent diffusion flame, Heat Transfer—Asian Research 39 (5) (2010) 292–313.

[45] Quintiere J, Harkleroad M. Hasemi Y. Wall flames and implications for upward flame spread, Combust. Sci. Technol. 1986;48:191–222.

[46] K.C. Tsai, Width effect on upward flame spread, Fire Safety J. 44 (2009) 962–967.

[47] Walters RN, SM Hackett, RE Lyon. Heats of combustion of high temperature polymers. Fire and Materials 2000;24:245–252.

[48] Lautenberger C, de Ris JL, Dembsey NA, Barnett JR, Baum HR. A simplified model for soot formation and oxidation in CFD simulation of non-premixed hydrocarbon flames. Fire Safety J 2005; 40:141–176.